Dual-Band Beam Scanning Antenna for the Satellite Ka-Band Based on Rotary Transmit Arrays

João Leandro Câmara Serra

***Abstract*— A polarization-insensitive dual-band beam scanning antenna using a rotary system with two transmit arrays is proposed in this work for small ground terminals in mobile broadband access in bi-directional satellite Ka-band applications. The challenge is combining high gain with a large scanning range, especially with dual-band systems. This work presents for the first time a dual-band polarization-insensitive implementation of the Risley Prism concept with TAs for two widely separated bands (20/30 GHz) and proposes a novel approach to define the phase correction of the lenses to improve the scanning performance. A set of 29 thin dual-band phase-delay unit cells is developed with transmission coefficient better than $-1\ dB$ at both bands, that covers all the required 20 and 30 GHz phase combinations. The TAs have a diameter $D = 144\ mm$, thickness $t = 3.233\ mm$, air gap separation of $d = 5\ mm$ and $F/D = 0.8$. Full-wave simulated gain is $25.6\ dBi$ at $f_1 \approx 20\ GHz$, $27.7\ dBi$ at $f_2 \approx 30\ GHz$ and a Sidelobe Level (SLL) of $-14.4\ dB$ at both bands for $\theta_{max} \approx 0°$. The scanning range is $[-50°, 50°]$ with a scan loss lower than $-3\ dB$ and $SLL < -10\ dB$. A prototype is being built and measured.**

***Index Terms*—Transmit Array, K/Ka-band, Dual-band, Beam Scanning, Risley Prism**

I. Introduction

In the last decade, there has been an increasing interest regarding applications involving beam scanning antennas: satellite-on-the-move (SOTM), point-to-multipoint, tracking, etc. They require the ability to perform elevation and azimuth beam steering as well as to present a high gain to compensate the Path Loss that is critical for long distance millimeter wave communications. In satellite communications, the Circular Polarization is the most common choice because it is less influenced by multipath fading effects, polarization mismatch due to the Faraday's Effect and the ground terminal mobility. The up-link and down-link use orthogonal polarizations and different frequency bands to reduce the interference between the transmitted and received signals.

The market of small ground terminals for mobile broadband access applications is expected to grow with the next generation of High Throughput Satellites (HTS) and High Altitude Platforms (HAP), so the challenge is to satisfy these requirements using a compact, low-profile, lightweight and low-cost solution that is appropriate for mass market production.

Beam scanning antennas can use different steering mechanisms: electronic solutions [1-5] based on phased arrays with a feeding system that is electronically controlled; mechanical solutions [6-10] relying on mechanical movements from the radiating aperture or from the feed; hybrid solutions [11] with electronical and mechanical components. The best choice depends on the problem characteristics and we have chosen a mechanical mechanism because it allows a wider scanning range, it is very cost-effective and it uses only one single feed, although it tends to be bulkier.

A transmit array (TA) [6, 7, 12] is a thin flat Phase Shifting Surface (PSS) lens discretized into unit cells. Inspired by reflect arrays [13-15], transmit arrays receive an incident wave and manipulate the propagation characteristics of the transmitted wave using predefined in-plane wave vectors. PSS technology is a low-cost, compact and low-weight alternative to dielectric edges [10, 16, 17].

The mechanical steering mechanisms of solutions involving TAs typically involve in-plane translations and/or rotations around the normal axis to reduce the antenna height. In-plane translation mechanisms are simpler because they only require one lens [6, 9] but they are associated with non-linear phase shifting errors that originate aberrations in the radiation pattern. The in-plane translation can be applied to the lens, which requires extra available space, or the feed, twisting the RF cable and damaging it in the long run. On the other hand, rotation solutions use two [7] or more [8] lenses which introduce losses, but they require less available space to operate.

Most satellite communication links are bi-directional, and each link uses a separate frequency band to minimize the inter-link interference. Additionally, in some applications like SOTM orthogonal circular polarizations are required between up-link and down-link, with the possibility of toggling the combination. This requires dual-band polarization-insensitive solutions that can operate simultaneously on two distinct bands instead of using one single-band solution for the up-link and another one for the down-link. The best option is to use dual-band phase-delay (PD) unit cells which can have different designs [6, 8, 18-20].

In the literature, there are already solutions performing beam steering using dual-band phase-delay transmit arrays [6, 20] or single-band Risley Prism-like rotation systems [7, 8] but the two were never combined before, as far as we know. In [8], a solution is proposed using 3 TAs (one for collimation and two

rotating lenses with tilting effects) and dual-band PD cells, however the gain is considerably low ($e_a \approx 25\%$ at $f = 8\ GHz$ and $e_a \approx 15\%$ at $f = 14\ GHz$) and it is not truly a dual-band Risley Prism-like system because the main lobe direction is not the same in both frequencies.

The design of a system with dual-band TAs based on the Risley Prism concept had three steps: first, a Physical Optics/Geometrical Optics (PO/GO) analysis to study and determine the main geometrical parameters with ideal phase distributions; then, a full-wave analysis in the Frequency Domain to design the dual-band PD cells; finally, a full-wave analysis in the Time Domain to evaluate the performance of the antenna. The PO/GO analysis was done using the KH3D_near program developed in house [22] and the full-wave analyses were made using CST software [23]. A prototype is being built and tested using a radio-frequency anechoic chamber to validate the previous analysis.

The antenna proposed in this work is the first dual-band beam scanning solution using a rotary system of transmit arrays. It is an extension of the Risley Prism concept, that allows pointing the beam at the same direction at two well-separated bands, like the satellite Ka-band. Besides, a new approach is proposed for the system design that ensures more stable radiation patterns than traditional designs. Our antenna presents high gain at both frequency bands and it guarantees a scanning range of $[-50°, 50°]$ with a scan loss smaller than $-3\ dB$.

This work is organized as follows. The geometry of our solution is introduced in Chapter II. Chapter III presents the unit cell design and characteristics. Chapter IV introduces the conventional and new phase distributions and compares the performance of the transmit arrays using each one. Finally, Chapter V has the main conclusions of this work.

II. Beam Scanning Mechanism

A. System Geometry

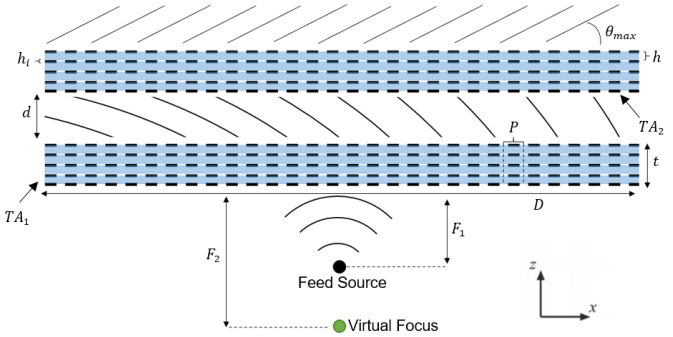

Figure 1 – Proposed mechanical beam steering solution: the qualitative wavefront propagation is represented using solid black lines.

The system proposed in this work consists of two rotatable Phase Shifting Surfaces working as TAs, TA_1 and TA_2, with some external feed source as shown in Figure 1. The feed source radiates a spherical wave that is transformed by TA_1 into a tilted spherical wave with a virtual focus that is further away from the lens than the actual feed focus. TA_2 collimates the incident wave, radiating a plane wave with an elevation angle θ_{max}.

Each TA has a circular geometry with diameter $D = 148\ mm$ and thickness $t = 3.233\ mm$. The two lenses have a concentric configuration and they are separated by an air gap with thickness $d = 5\ mm$. The origin of the (x, y, z) coordinate system is the feed phase center.

To perform beam scanning, it is always necessary to ensure at least two degrees of freedom, because an arbitrary direction is defined by two parameters: the elevation angle θ and the azimuth angle φ. In our solution, this is achieved thanks to the independent rotation of the two lenses around the $\hat{\boldsymbol{z}}$ axis defined by ψ_1 and ψ_2. Figure 2 shows the in-plane rotation system.

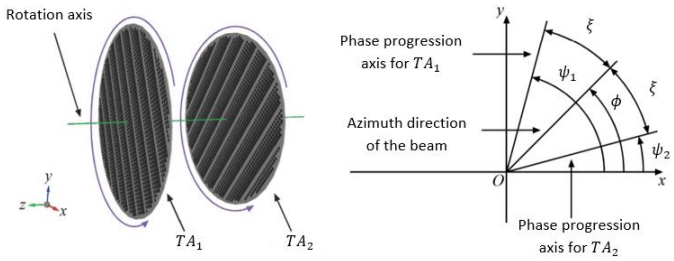

Figure 2 – Rotation mechanism seen from perspective (left) and rotation coordinate system seen from above (right): ψ_1 and ψ_2 are the rotation angles of the progression axes of TA_1 and TA_2, respectively. This figure was taken from [7].

B. Phase Distributions

The phase transmission distributions of a TA is defined as

$$\phi_{lens}(x, y) = \phi_{out}(x, y) - \phi_{in}(x, y) \tag{1}$$

where ϕ_{in} and ϕ_{out} are the phase distributions over the incidence and transmission surfaces, respectively.

For a spherical wave feed source, the phase distribution over the incidence surface of TA_1 is simply given by

$$\phi_{in,1}(x, y) = k_0\sqrt{x^2 + y^2 + F_1^2} \tag{2}$$

and the distribution over the transmission surface for a tilted spherical wave along the $(\theta = \alpha_1, \varphi = \psi_1)$ direction with a virtual focus distance F_2 is

$$\phi_{out,1}(x, y) = k_0\left[\sqrt{x^2 + y^2 + F_2^2} + \sin\alpha_1\,(\cos\psi_1\, x + \sin\psi_1\, y)\right] \tag{3}$$

Therefore, the phase transmission distribution of TA_1 is

$$\phi_{lens,1}(x, y) = k_0\left[\sqrt{x^2 + y^2 + F_2^2} - \sqrt{x^2 + y^2 + F_1^2} + \sin\alpha_1\,(\cos\psi_1\, x + \sin\psi_1\, y)\right] + k_0(F_1 - F_2) \tag{4}$$

where $k_0(F_1 - F_2)$ is a phase zeroing term that does not affect the lens performance because a phase distribution is uniquely defined apart from an additive spatially constant term that may vary with frequency.

The incident wave over TA_2 is the transmitted wave by TA_1, so $\phi_{in,2}(x, y, z) = \phi_{out,1}(x, y, z + d)$, that is,

$$\phi_{in,2}(x, y) = k_0 \left[\sqrt{x^2 + y^2 + (F_2 + d)^2} + \sin\alpha_1 \left(\cos\psi_1\, x + \sin\psi_1\, y\right)\right] \quad (5)$$

Since $d \ll F_2$, for simplicity we can approximate the incident wave as

$$\phi_{in,2}(x, y) \approx k_0 \left[\sqrt{x^2 + y^2 + F_2^2} + \sin\alpha_1 \left(\cos\psi_1\, x + \sin\psi_1\, y\right)\right] \quad (6)$$

The phase transmission distribution of TA_2 is

$$\phi_{lens,2}(x, y) = k_0 \left[-\sqrt{x^2 + y^2 + F_2^2} + \sin\alpha_2 \left(\cos\psi_2\, x + \sin\psi_2\, y\right)\right] + k_0 F_2 \quad (7)$$

where $k_0 F_2$ is another phase zeroing term. Therefore, the phase distribution of over the transmission surface of TA_2 is

$$\phi_{out,2}(x, y) = k_0([\sin\alpha_1 \cos\psi_1 + \sin\alpha_2 \cos\psi_2]x + [\sin\alpha_1 \sin\psi_1 + \sin\alpha_2 \sin\psi_2]y) \quad (8)$$

If $\alpha_1 = \alpha_2 = \alpha_0$ and if we substitute $\psi_1 = \phi + \xi$ and $\psi_2 = \phi - \xi$ in (7), we get

$$\phi_{out,2}(x, y) = k_0[\sin\theta_{RP} \left(\cos\phi\, x + \sin\phi\, y\right)] \quad (9)$$

Since $\phi_{out,2} = \phi_{out}$, the system radiates a plane wave propagating along the $(\theta = \theta_{RP}, \varphi = \phi)$ as intended, where $\theta_{RP} = |\arcsin(2\sin\alpha_0 \cos\xi)|$. Thus, this Risley Prism implementation can perform beam scanning: the elevation angle is controlled by the differential rotation angle ξ and the azimuth angle by the mean rotation angle ϕ.

The greatest challenge is to accomplish this behaviour simultaneously in two well-separated frequency bands, while ensuring the same pointing direction in the two bands.

III. Dual-Band PD Unit Cells

As explained in the Introduction, each TA is discretized into multiple unit cells. These cells should have good transmission amplitudes and a small phase discretization step. Each cell has an in-plane width $P = 3.5\ mm$ and it has 5 layers with metallic inductive elements (small black rectangles in Figure 1) interleaved with 4 dielectric layers (blue rectangles in Figure 1) as shown in Figure 3. Each metallic layer has 2 or 3 concentric square copper rings (the number of rings varies from layer to layer in each cell) with thickness $h_i = 0.017\ mm$. The dielectric layers have thickness $h = 0.787\ mm$ and they are made of Rogers RT5880 ($\varepsilon_r = 2.2, \tan\delta = 0.0009$). This design was inspired by the PG TA cells presented in [8].

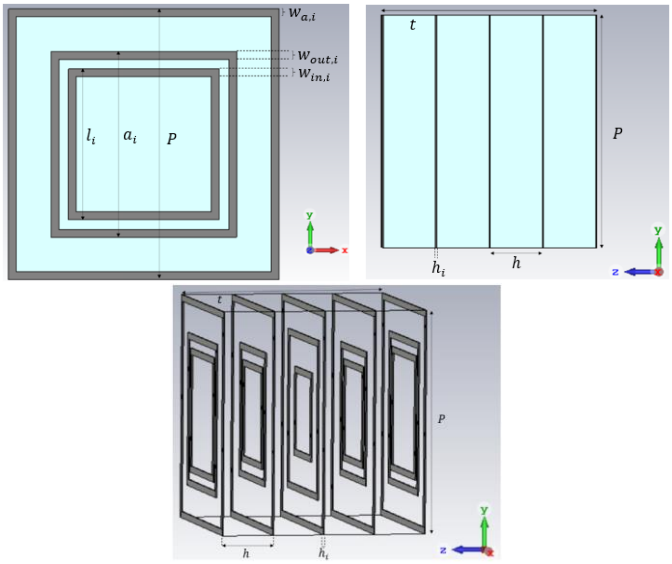

Figure 3 – Dual-band PD unit cell's design model: the square metal rings are represented in dark grey and the dielectric layers in light green; the layer's number label decreases with z. Up: front (left) and side (right) view of a cell. Down: 5 layers of metal elements without the dielectric layers

The phase transmission distributions discussed in the previous chapter vary in space but also in frequency because $k_0 = 2\pi f/c$. To ensure the TAs have the exact same effect over the incident wave at both bands, they must satisfy the following relation:

$$\phi_{lens,i}(x, y, f_2) - \phi_{f_2}^{ref} = \frac{f_2}{f_1}\left(\phi_{lens,i}(x, y, f_1) - \phi_{f_1}^{ref}\right) \quad (10)$$

To reduce the number of cells necessary to populate the phase range, it is common to use phase wrapping [6]: phase is a 360° periodic function, it is only necessary to populate one periodic phase range. While in single-band lenses the periodic range is $[0°, 360°[$, in dual-band problems this is not so simple because each band will have a periodic range that is different from the other. If we can define the phase transmission of the cell i as $\phi_f^i = \phi_{lens}(x_i, y_i, f) - \phi_f^{ref}$, where (x_i, y_i) are the coordinates of its center, each dual-band unit cell i must satisfy

$$\phi_{f_2}^i + n \times 360° = \frac{f_2}{f_1}\left(\phi_{f_1}^i + m \times 360°\right) \quad (11)$$

where $n, m \in \mathbb{Z}$. To minimize the phase range in each band, f_1 and f_2 should be chosen as the pair of frequencies from both

bands that have integer values and present the maximum greatest common divisor [6]. For satellite Ka-band applications, one should define $f_1 = 20\ GHz$ and $f_2 = 30\ GHz$.

29 thin dual-band PD cells were designed using full-wave analysis in the Frequency Domain using the CST software [23] for a normal incident plane wave with Linear Polarization and periodic boundaries. Figures 4 and 5 show the transmission amplitude and phase of these cells for the pair of phase references $\left(\phi_{f_1}^{ref} = -80°, \phi_{f_2}^{ref} = -22.5°\right)$ that minimize the mean phase error.

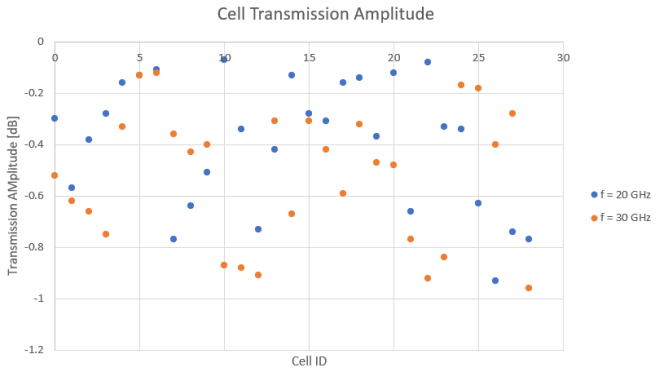

Figure 4 – Transmission amplitude of each cell at $f_1 = 20\ GHz$ (blue) and $f_2 = 30\ GHz$ (orange). Some cells have the same transmission amplitude in both frequencies, so it is only possible to see the f_2 data

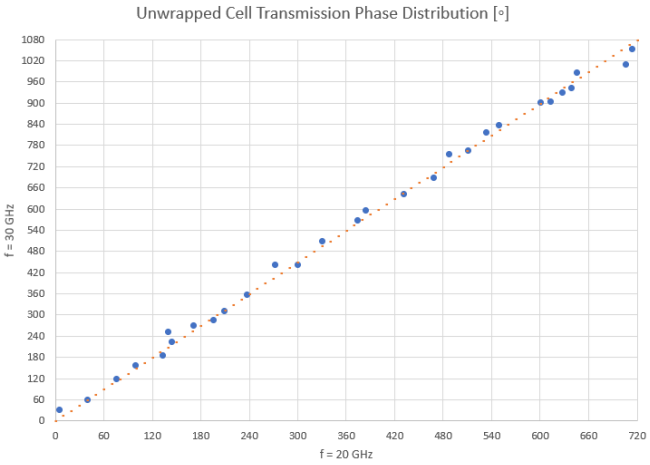

Figure 5 – Transmission phase of each cell: in orange, the graphical representation of relation (10); in blue, the cells' transmission phase distribution. The lowest phase corresponds to $ID = 0$ and the highest to $ID = 28$

Every cell has a transmission amplitude better than $-1\ dB$, the mean phase error is 9.3° at $f_1 = 20\ GHz$ and 13.9° at $f_2 = 30\ GHz$ and the mean phase discretization step is 24.8° at $f_1 = 20\ GHz$ and 37.2° at $f_2 = 30\ GHz$.

IV. Dual-Band Transmit Arrays

A. Equivalent Dielectric Description

The performance of the TAs with the previous dual-band PD unit cells was studied through a full-wave analysis using the Time Domain tool of CST software. The square metallic rings of the cells have very small dimensions that require an extremely thin Mesh to properly discretize the lenses. This makes the simulation process incredibly complex in terms of time and resources, so the dual-band cells were replaced by equivalent dielectric single-band cells [21] with the same dimensions P and t and the same transmission coefficients at both bands. Note that the unit cell sub-wavelength assumption of the Homogenization Theory is verified because $P < \lambda_0/2$, where λ_0 is the free-space wavelength. The equivalent cell i at frequency f has the following relative electric parameters:

$$\varepsilon_{eq,f}^{i} = -\frac{\phi_f^i + \phi_f}{k_0 t}\frac{1+\left|\Gamma_f^i\right|}{1-\left|\Gamma_f^i\right|}$$
$$\mu_{eq,f}^{i} = -\frac{\phi_f^i + \phi_f}{k_0 t}\frac{1-\left|\Gamma_f^i\right|}{1+\left|\Gamma_f^i\right|} \quad (12)$$

where Γ_f^i is the reflection coefficient of cell i at frequency f and ϕ_f is an arbitrary phase constant that guarantees $\varepsilon_{eq,f}^{i}, \mu_{eq,f}^{i} \geq 1$ for $i = 0, \ldots, 28$. To reduce the simulation volume, the external feed source (Horn antenna) was replaced by equivalent feed sources.

B. Conventional Phase Distributions

Previous works with Risley Prism concepts [7, 8] use a conventional pair of transmission phase distributions of the lenses without a virtual focus:

$$\phi_{usual,1}(x,y) = k_0\left[-\sqrt{x^2+y^2+F_1^2} + \sin\alpha_0\left(\cos\psi_1\, x + \sin\psi_1\, y\right)\right] + k_0 F_1 \quad (13)$$

$$\phi_{usual,2}(x,y) = k_0 \sin\alpha_0\left(\cos\psi_2\, x + \sin\psi_2\, y\right) \quad (14)$$

Note that removing the virtual focus is equivalent to consider an infinitely distant focus, that is: $\phi_{usual,i} = \lim_{F_2\to\infty} \phi_{lens,i}$. Figure 6 shows the equivalent lenses for these phase distributions with $F_1 = 100\ mm$, $\alpha_0 = 25°$ and $\psi_1 = \psi_2 = 0°$.

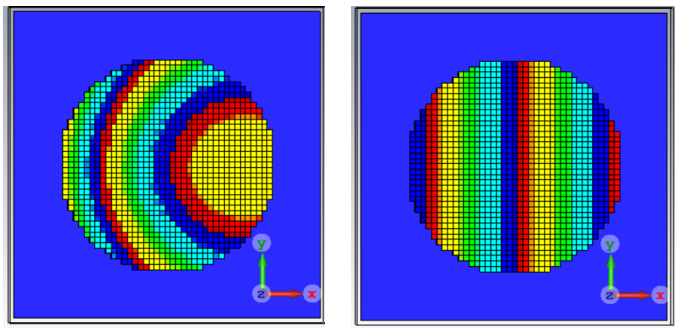

Figure 6 – Equivalent dielectric Lens 1 (left) and Lens 2 (right) defined by the conventional phase distributions (13) and (14). The blue screen behind each lens is the respective equivalent feed source

With these conventional distributions, TA_1 collimates the incident wave and transmits a tilted plane wave and TA_2 only

tilts once again the incident plane wave. Figures 7-8 and Table 1 show the far-field results of each lens at f_1 and f_2 with $F_1 = 100\,mm$ and $\psi_1 = \psi_2 = 0°$ for two different values of the offset elevation angle α_0.

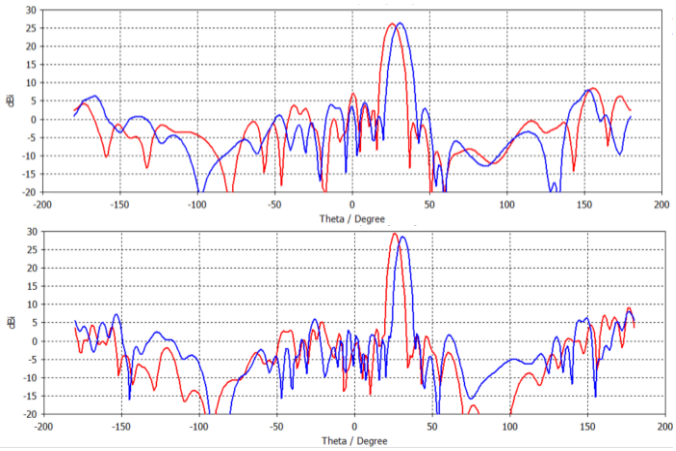

Figure 7 – $\varphi = 0°$ Directivity cut for Lens 1 at $f_1 = 20\,GHz$ (above) and $f_2 = 30\,GHz$ (below) using the conventional phase distributions with $F_1 = 100\,mm$ and $\psi_1 = 0°$ for different values of α_0: 25° (red), 30° (blue)

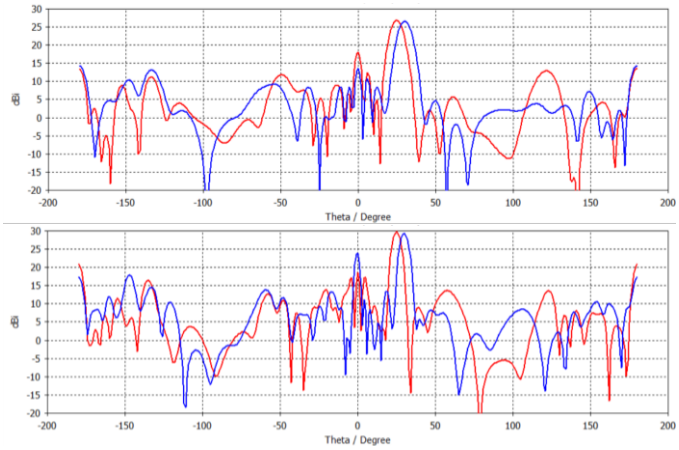

Figure 8 – $\varphi = 0°$ Directivity cut for Lens 2 at $f_1 = 20\,GHz$ (above) and $f_2 = 30\,GHz$ (below) using the conventional phase distributions with $F_1 = 100\,mm$ and $\psi_2 = 0°$ for different values of α_0: 25° (red), 30° (blue)

Table 1 – Far-field results of Lens 1 using the conventional phase distributions at both bands with $F_1 = 100\,mm$ for different values of α_0

α_0 [°]	D_{max} [dBi]		SLL [dB]		θ_{max} [°]	
	f_1	f_2	f_1	f_2	f_1	f_2
25	26.2	29.5	-17.7	-20.3	26	26
30	26.4	28.6	-18.4	-20.7	31	31

Table 2 – Far-field results of Lens 2 using the conventional phase distributions with $F_1 = 100\,mm$ for different values of α_0

α_0 [°]	D_{max} [dBi]		SLL [dB]		θ_{max} [°]	
	f_1	f_2	f_1	f_2	f_1	f_2
25	26.8	29.7	-8.8	-8.9	25	25
30	26.5	29.4	-12.2	-5.4	30	30

Both lenses radiate a tilted plane wave with $\theta_{max} = \alpha_0$ as expected. The performance of Lens 1 is very good but the Radiation Pattern of Lens 2 presents transmitted and reflected side lobes with high magnitudes at $\theta = 0°$ and $\theta = 180°$, specially at $f_2 = 30\,GHz$. Since both lenses use the same set of cells, this effect must be related to the phase distributions. Our suspicion is that the equivalent surface currents [24] are a linear combination of Floquet modes, due to the periodic nature of the phase distribution of Lens 2, with second-order effects that may generate constructive interference in some cases like ours, originating the transmitted and reflected side lobes. Curiously, we have not found this effect mentioned in similar works, so probably it arises from some unlucky combination of phase distribution (14) and our particular set of cells, despite being a valid one.

C. New Proposed Phase Distributions

The new proposed phase distributions (4) and (7) appear as an alternative approach to deal with the problem discussed in the previous section: the periodicity of Lens 2 disappears by creating a virtual focus, which introduces a radial term. Figure 9 shows the new pair of equivalent lenses with $F_1 = 100\,mm$, $F_2 = 150\,mm$, $\alpha_0 = 25°$ and $\psi_1 = \psi_2 = 0°$.

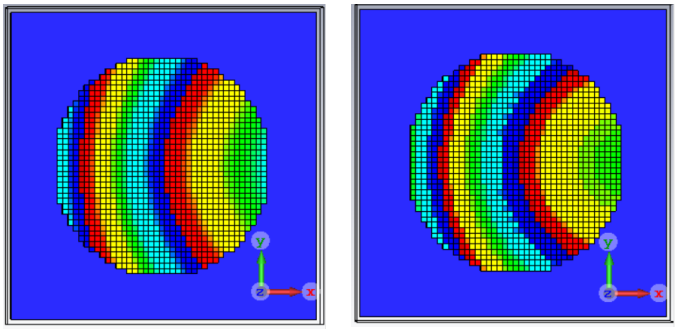

Figure 9 – Equivalent dielectric Lens 1 (left) and Lens 2 (right) for the new phase distributions (4) and (7) with $F_1 = 100\,mm$, $F_2 = 150\,mm$, $\alpha_0 = 25°$ and $\psi_1 = \psi_2 = 0°$. The blue screen behind each lens is the equivalent feed source

The Directivity of an aperture with surface area A and aperture efficiency e_a radiating wave with an elevation angle θ_{max} for a frequency f is

$$D_{max} = \frac{4\pi A}{\lambda^2} e_a \cos\theta_{max} \qquad (15)$$

Since each lens radiates a wave with $\theta_{max} = \alpha_0$, it was defined the elevation angle offset as $\alpha_0 = 25°$ to improve the Directivity. Also, $\alpha_0 = 25°$ allows a theoretical Risley Prism scanning range $\theta_{RP} \in [-50°, 50°]$, which satisfies the requirements of most applications. The focal distance of the feed source was defined as $F_1 = 100\,mm$ to ensure a Taper Level close to $-10\,dB$ over TA_1. Figures 10-11 and Table 3 show the far-field results for the two lenses system using the new phase distributions (4) and (7) at both bands with $F_1 = 100\,mm$, $\alpha_0 = 25°$, $d = 5\,mm$ and $\theta_{RP} = 0°$ for different values of the virtual focus distance F_2.

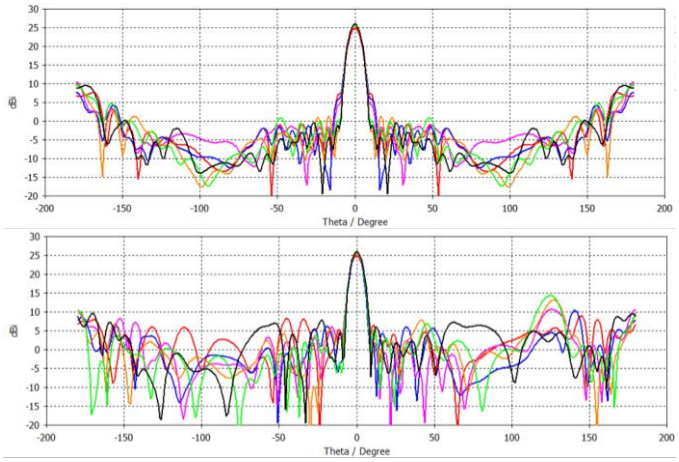

Figure 10 – $\varphi = 0°$ (above) and $\varphi = 90°$ (below) Directivity cuts for the 2 equivalent lenses system at $f_1 = 20\ GHz$ using the new phase distributions with $F_1 = 100\ mm$, $\alpha_0 = 25°$, $d = 5\ mm$ and $\theta_{RP} = 0°$ for different values of F_2: 100 mm (red), 125 mm (blue), 150 mm (purple), 175 mm (orange), 200 mm (green) and ∞ (black)

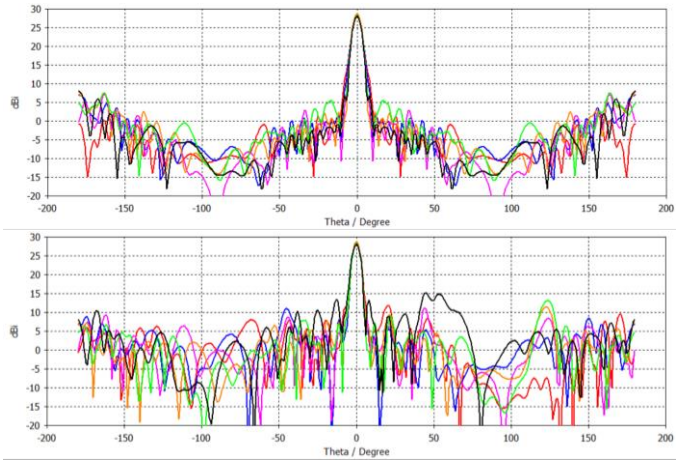

Figure 11 – $\varphi = 0°$ (above) and $\varphi = 90°$ (below) Directivity cuts for the 2 equivalent lenses system at $f_2 = 30\ GHz$ using the new phase distributions with $F_1 = 100\ mm$, $\alpha_0 = 25°$, $d = 5\ mm$ and $\theta_{RP} = 0°$ for different values of F_2: 100 mm (red), 125 mm (blue), 150 mm (purple), 175 mm (orange), 200 mm (green) and ∞ (black)

Table 3 – Far-field results of the 2 equivalent lenses system using the new phase distributions at both bands with $F_1 = 100\ mm$, $\alpha_0 = 25°$, $d = 5\ mm$ and $\theta_{RP} = 0°$ for different values of F_2

$\mathbf{F_2}\ [mm]$	$D_{max}\ [dBi]$		e_a [%]		$SLL\ [dB]$	
	f_1	f_2	f_1	f_2	f_1	f_2
100	24.9	28.3	35.9	34.9	-15.9	-16.6
125	25.5	28.5	41.3	36.6	-15.2	-17.5
150	25.5	28.6	41.3	37.4	-14.8	-17.4
175	25.6	28.8	42.2	39.2	-12.4	-17.4
200	25.8	28.2	44.2	34.2	-11.5	-15.1
∞	26.0	28.1	46.3	33.4	-16.5	-12.9

We have used three criteria to compare the different results: maximize the aperture efficiency, minimize the Sidelobe Level and maximize the worst case between the two bands. The virtual focus distance was defined as $F_2 = 150\ mm$ because it provides the best results. If we compare these results with the conventional phase distributions ($F_2 \to \infty$), the Directivity decreases 0.5 dB and the SLL increases 1.7 dB at $f_1 = 20\ GHz$, and the Directivity increases 0.5 dB and the SLL improves 4.5 dB at $f_2 = 30\ GHz$. Curiously, $F_2 = 100\ mm$ also corresponds to the conventional phase distributions if we switch the order of the lenses and the results at $f_2 = 30\ GHz$ improve as well. It seems that Lens 1 transmitting a spherical wave, instead of a plane wave, makes the side lobe energy spread out, explaining the impact over the SLL.

Table 4 presents the far-field results for the two lenses system using the new phase distributions (4) and (7) at both bands with $F_1 = 100\ mm$, $F_2 = 150\ mm$, $\alpha_0 = 25°$ and $\theta_{RP} = 0°$ for different values of the air gap thickness d.

Table 4 – Far-field results of the 2 equivalent lenses system using the new phase distributions at both bands with $F_1 = 100\ mm$, $F_2 = 150\ mm$, $\alpha_0 = 25°$ and $\theta_{RP} = 0°$ for different values of d

$d\ [mm]$	$D_{max}\ [dBi]$		e_a [%]		$SLL\ [dB]$	
	f_1	f_2	f_1	f_2	f_1	f_2
2.5	25.8	27.8	44.2	31.1	-16.2	-16.3
5.0	25.5	28.6	41.3	37.4	-14.8	-17.4
7.5	25.8	28.1	44.2	33.4	-18.5	-15.8

Using the same criteria as before, the air gap thickness was defined as $d = 5.0\ mm$.

D. Scanning Performance

Besides presenting high gain, a beam scanning antenna should have a large scanning range. The scanning range is defined as the elevation angle range where the scan loss is better or equal than $-3\ dB$ and $SLL \leq -10\ dB$. Figure 12 and Table 5 show the scanning performance of our equivalent system. Figure 13 and Table 5 show the scanning performance for the conventional phase distributions for comparison.

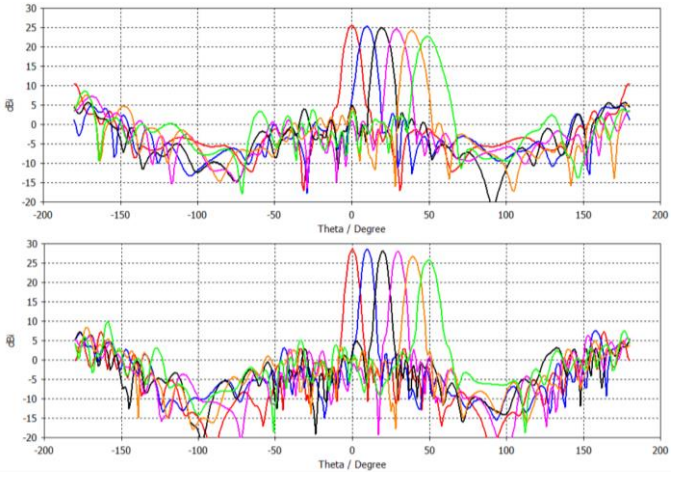

Figure 12 – Scanning performance of the 2 equivalent lenses system at $f_1 = 20\ GHz$ (above) and $f_2 = 30\ GHz$ (below) using the new phase distributions with $F_1 = 100\ mm$, $F_2 = 150\ mm$, $\alpha_0 = 25°$ and $d =$

5 mm for different scanning angles θ_{RP}: 0° (red), 10° (blue), 20° (black), 30° (purple), 40° (orange) and 50° (green)

Table 5 – Scanning performance of the 2 equivalent lenses system at both bands using the new phase distributions with $F_1 = 100\ mm$, $F_2 = 150\ mm$, $\alpha_0 = 25°$ and $d = 5\ mm$

D_{max} [dBi]		SLL [dB]		θ_{max} [°]		φ_{max} [°]	
f_1	f_2	f_1	f_2	f_1	f_2	f_1	f_2
25.5	28.6	-14.8	-17.4	2	2	-90	-90
25.3	28.6	-13.5	-19.5	10	10	-11	-9
24.9	28.2	-13.8	-19.5	19	20	-5	-5
24.6	28.0	-12.8	-19.5	29	29	-3	-3
24.3	26.7	-12.4	-17.6	39	39	-2	-2
22.7	25.7	-11.1	-15.3	49	49	-2	-2

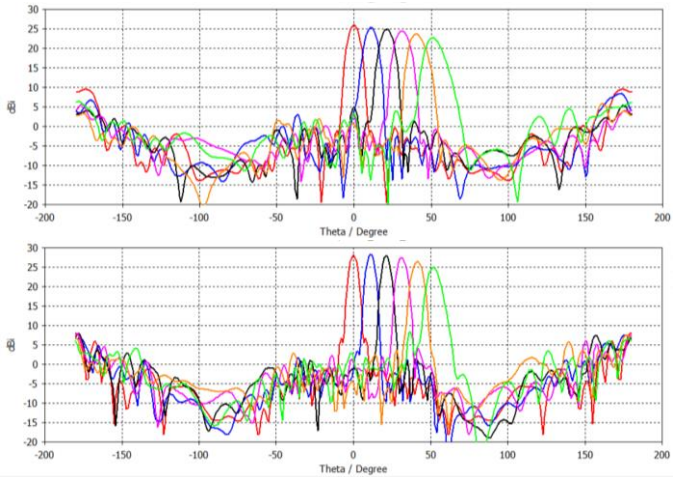

Figure 13 – Scanning performance of the 2 equivalent lenses system at $f_1 = 20\ GHz$ (above) and $f_2 = 30\ GHz$ (below) using the new phase distributions with $F_1 = 100\ mm$, $\alpha_0 = 25°$ and $d = 5\ mm$ for different scanning angles θ_{RP}: 0° (red), 10° (blue), 20° (black), 30° (purple), 40° (orange) and 50° (green)

Table 6 – Scanning performance of the 2 equivalent lenses system at both bands using the conventional phase distributions with $F_1 = 100\ mm$, $\alpha_0 = 25°$ and $d = 5\ mm$

D_{max} [dBi]		SLL [dB]		θ_{max} [°]		φ_{max} [°]	
f_1	f_2	f_1	f_2	f_1	f_2	f_1	f_2
26.0	28.1	-16.5	-12.9	1	1	90	90
25.3	28.4	-16.7	-13.4	11	11	4	3
24.9	28.0	-17.0	-12.5	21	21	2	1
24.4	27.4	-16.8	-13.7	31	31	1	1
23.6	26.5	-13.1	-11.2	40	42	0	0
22.7	25.0	-9.3	-10.8	51	52	-1	0

The SLL values from Tables 5 and 6 do not correspond to Figures 12 and 13 because the most prominent side lobes are not aligned with the main lobe direction. At $\theta_{max} \approx 50°$, our solution has a scan loss of $-2.8\ dB$ and a $SLL = -11.1\ dB$ at $f_1 = 20\ GHz$ and a scan loss of $-2.9\ dB$ and a $SLL = -15.3\ dB$ at $f_2 = 30\ GHz$, so the scanning range is $\theta_{max} \in [-50°, 50°]$. On the other hand, at $\theta_{max} \approx 50°$, the system using the conventional phase distributions has a scan loss of $-3.3\ dB$ and a $SLL = -9.3\ dB$ at $f_1 = 20\ GHz$ and a scan loss of $-3.1\ dB$ and a $SLL = -10.8\ dB$ at $f_2 = 30\ GHz$, so the scanning range is only $\theta_{max} \in [-40°, 40°]$. Also, at $\theta_{max} \approx 50°$, our system has the same Directivity as the conventional solution at $f_1 = 20\ GHz$ and a $0.7\ dB$ gain at $f_2 = 30\ GHz$, besides a significant improvement regarding the SLL. Therefore, our solution presents better results than the conventional system.

Even though both systems present a shift regarding the azimuth direction of the main lobe φ_{max}, this is not problematic because that can always be corrected by controlling the mean rotation angle ϕ.

E. Equivalent Analysis Validation

We have studied our system using an equivalent dielectric description of the cells and, although it has been shown to provide accurate results [21], there are coupling effects between cells from the same lens and between the two lenses that cannot be described by dielectric cells. Therefore, the previous analysis must be validated using the real dual-band PD cells shown in Figure 14.

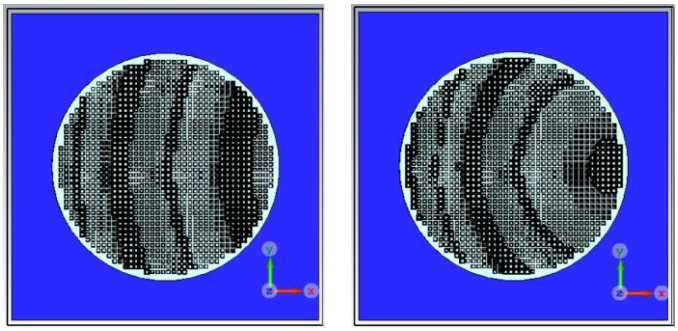

Figure 14 – Real Lens 1 (left) and Lens 2 (right) defined by the new phase distributions (4) and (7) with $F_1 = 100\ mm$, $F_2 = 150\ mm$, $\alpha_0 = 25°$ and $\psi_1 = \psi_2 = 0°$. The dielectric layers are coloured in light green and the metallic layers are coloured in dark grey. The blue screen behind each lens is the equivalent feed source.

We have simulated the two lenses system for $\theta_{RP} = 0°$ and the best results appear at $f_1 = 20.3\ GHz$ and $f_2 = 29.9\ GHz$. Figures 15 – 16 and Table 7 show these results.

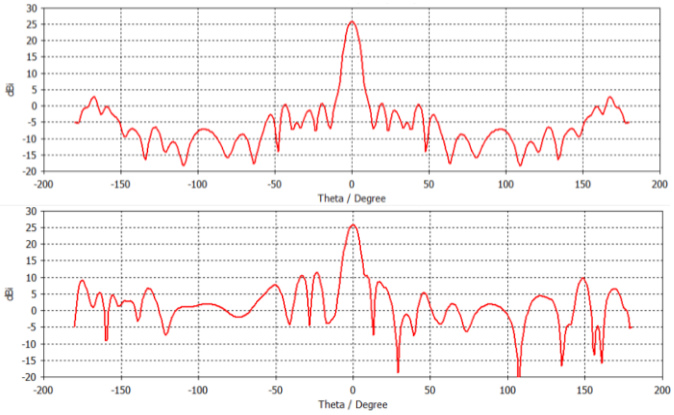

Figure 15 – $\varphi = 0°$ (above) and $\varphi = 90°$ (below) Directivity cuts for the two real lenses at $f_1 = 20.3\ GHz$ using the new phase distributions with $F_1 = 100\ mm$, $F_2 = 150\ mm$, $\alpha_0 = 25°$, $d = 5\ mm$ and $\theta_{RP} = 0°$

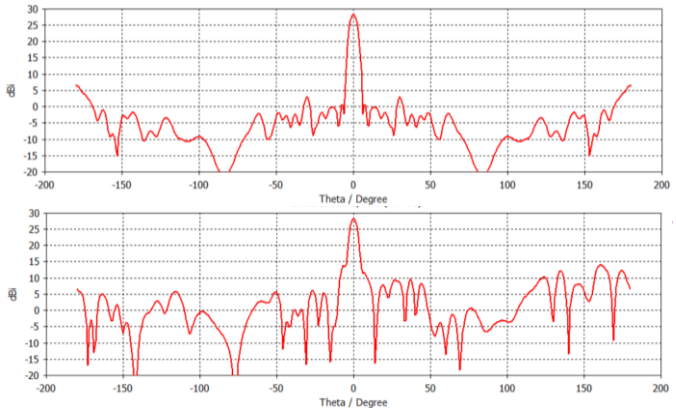

Figure 16 – $\varphi = 0°$ (above) and $\varphi = 90°$ (below) Directivity cuts for the two real lenses at $f_2 = 29.9\ GHz$ using the new phase distributions with $F_1 = 100\ mm$, $F_2 = 150\ mm$, $\alpha_0 = 25°$, $d = 5\ mm$ and $\theta_{RP} = 0°$

Table 7 – Far-field results comparison for the 2 real and equivalent lenses system at both bands using phase distributions (24) and (26) with $F_1 = 100\ mm$, $F_2 = 150\ mm$, $\alpha_0 = 25°$, $d = 5\ mm$ and $\theta_{RP} = 0°$

Lenses	D_{max} $[dBi]$		SLL $[dB]$		θ_{max} [°]	
	f_1	f_2	f_1	f_2	f_1	f_2
Equivalent	25.5	28.6	-14.8	-17.4	2	2
Real	25.9	28.3	-14.4	-14.4	1	1

The results from the real lenses are very similar to the ones obtained with the equivalent dielectric descriptions shown in Table 4, thereby validating the previous analysis. We have only used the $\theta_{RP} = 0°$ scenario to explore the symmetry regarding the $y0z$ plane, which significantly reduces the simulation time. Even for this special case, the simulation time was 37 hours due to the very thin Mesh.

The antenna efficiency was calculated by comparing the total radiated power from the equivalent feed source alone and with the rotary system. The corresponding gain is $G = 25.6\ dBi$ at $f_1 = 20.3\ GHz$ and $G = 27.7\ dBi$ at $f_2 = 29.9\ GHz$.

V. Conclusion

A dual-band polarization-insensitive beam scanning antenna using a Risley Prism-like rotation system with two transmit arrays was successfully designed for the first time. This antenna is intended for small ground terminals in mobile broadband access applications in satellite Ka-band (Rx: $20\ GHz$, Tx: $30\ GHz$), such as High Throughput Satellites and High Altitude Platforms. The prototype is being built and tested.

29 thin dual-band phase-delay unit cells were designed with a transmission amplitude better than $-1\ dB$ at both bands. The lenses have a diameter $D = 148\ mm$, a thickness $t = 3.233\ mm$, they are separated by an air gap $d = 5\ mm$ and the feed source is a Horn Antenna with a focal distance $F_1 = 100$ mm, which means $F/D = 0.8$.

It is shown the conventional phase distributions of the lenses used in previous works with Risley Prisms concepts may introduce some limitations in the far-field results regarding the SLL and scanning range. Also, it is proposed a new pair of phase distributions with a virtual focus that improves the system's performance.

The antenna presents a gain $G = 25.6\ dBi$ at $f_1 = 20.3\ GHz$ and $G = 27.7\ dBi$ at $f_2 = 29.9\ GHz$. The scanning range is $\theta_{max} \in [-50°, 50°]$ with a scan loss better than $-3\ dB$ and $SLL < -10\ dB$ at both bands.

Acknowledgement

I would like to thank my supervisors, C. A. Fernandes and S. A. Matos, for their help, guidance and time throughout this work. Also, I would like to thank J. Felício for prototype construction and measurements, as well as for experimental advices, and C. Brito and J. Farinha for prototype construction. I would like to thank Instituto de Telecomunicacões (IT), UIDB/50008/2020, and project ADAM3D: PTDC/EEITEL/30323/2017, for financing all the needed material used in this thesis, and for the usage of IT laboratories, software and hardware equipment.

References

[1] S. Ye, X. Liang, W. Wang, R. Jin, J. Geg, T. S. Bird, Y. J. Guo, "High-Gain Planar Antenna Arrays for Mobile Satellite Communications", *IEEE Trans. Antennas Propag.*, vol. 54, no. 6, pp. 256-268, Dec. 2012.

[2] R. V. Gatti, L. Marcaccioli, E. Sbarra, R. Sorrentino, "Flat Array Antenna for Ku-Band Mobile Satellite Terminals", *Proc. 5th European Conf. Antennas and Propag. (EuCAP)*, pp. 2618-2622, Rome, Italy, Apr. 2011.

[3] Y. J. Cheng, P. Chen, W. Hong, T. Djerafi, K. Wu, "Substrate Integrated-Waveguide Beamforming Networks and Multibeam Antenna Arrays for Low-Cost Satellite and Mobile Systems", *IEEE Antennas and Propag. Mag.*, vol. 53, no. 6, pp. 18-30, Dec. 2011.

[4] L. A. Greda, A. Dreher, "Tx-Terminated Phased Array for Satellite Communication at Ka-Band", in *Proc. 37th European Microwave Conf.*, pp. 266-269, Munich, Germany, Oct. 2007.

[5] Y. Sheng, L. Xianling, W. Wenzhi, J. Ronghong, G. Junping, T. S. Bird, Y. J. Guo, "High-Gain Planar Antenna Arrays for Mobile Satellite Communications", *IEEE Antennas and Propag. Mag.*, vol. 54, no. 6, pp. 256-268, Dec. 2012.

[6] S. A. Matos, E. B. Lima, J. S. Silva, J. R. Costa, C. A. Fernandes, N. J. G. Fonseca, J. R. Mosig, "High Gain Dual-Band Beam-Steering Transmit Array for Satcom Terminals at Ka-Band", *IEEE Trans. Antennas Propag.*, vol. 65, no. 7, pp. 3528-3539, Jul. 2017.

[7] N. Gagnon, A. Petosa, "Using Rotatable Planar Phase Shifting Surfaces to Steer a High-Gain Beam", *IEEE Trans. Antennas Propag.*, vol. 61, no. 6, pp. 3086-3092, Jun. 2013.

[8] Q. Zeng, Z. Xue, W. Ren, W. Li, "Dual-Band Beam-Scanning Antenna Using Rotatable Planar Phase Gradient Transmit Arrays", *IEEE Trans. Antennas Propag.*, vol. 68, no. 6, pp. 5021-5026, Jan. 2020.

[9] E. B. Lima, S. A. Matos, J. R. Costa, C. A. Fernandes, N. J. G. Fonsced, "Circular Polarization Wide-angle Beam Steering at Ka-Band by In-plane Translation of a Plate Lens Antenna", *IEEE Trans. Antennas Propag.*, vol. 63, no. 12, pp. 5443-5455, Oct. 2015.

[10] J. R. Costa, C. A. Fernandes, G. Godi, R. Sauleau, L. Le Coq, H. Legay, "Compact Ka-Band Lens Antennas for LEO Satellites", *IEEE Trans. Antennas and Propag.*, vol. 56, pp. 1251-1258, May 2008.

[11] M. Tripodi, F. DiMarca, T. Cadili, C. Mollura, F. DiMaggio, M. Russo, "Ka Band Active Phased Array Antenna System for Satellite Communication on the Move Terminal", *Proc. 5th European Conf. Antennas and Propag. (EuCAP)*, pp. 2628-2630, Rome, Italy, Apr. 2011.

[12] X. Zhang, F. Yang, S. Xu, A. Aziz, M. Li, "Dual-Layer Transmitarray Antenna with High Transmission Efficiency", *IEEE Trans. Antennas Propag.*, vol. 68, no. 8, pp. 6003-6012, Aug. 2020.

[13] G. Bellaveglia, L. Marcellini, R. Lo Forti, A. Arcidiacono, B. Ray, "Low Profile Ku-Band VSAT Antenna System for High-Speed Trains", *29th ESA Antenna Workshop on Multiple Beams and Reconfigurable Antennas*, ESA/ESTEC Noorwijk, Netherland, May 2007.

[14] D. Martinez-de-Rioja, E. Martinez-de-Rioja, J. A. Encinar, A. Pino, Y. Rodriguez-Vaqueiro, B. Gonzalez-Valdes, O. Rubiños, M. Arias, "Single

and Dual Configurations for Multibeam Satellite Antennas in Ka-Band", *13th European Conf. Antennas and Propag. (EuCAP)*, 2019.

[15] G. Wu, S. Qu., S. Yang, "Wide-Angle Beam-Scanning Reflectarray with Mechanical Steering", *IEEE Trans. Antennas Propag.*, vol. 66, no. 1, pp. 172-181, Jan. 2018.

[16] A. A. Baba, R. M. Hashmi, K. P. Esselle, M. Attygalle, D. Borg, "A Millimeter-Wave Antenna System for Wideband 2-D Beam Steering", *IEEE Trans. Antennas and Propag.*, vol. 68, no. 5, May 2020.

[17] T. Maruyama, K. Yamamori, Y. Kuwahara, "Design of Multibeam Dielectric Lens Antennas by Multiobjective Optimization", *IEEE Trans. Antennas Propag.*, vol. 57, no. 57-63, Jan. 2009.

[18] A. Ebrahimi, W. Withayachumnankul, S. Al-Sarawi, D. Abbott, "Design of dual-band frequency selective surface dual band unit cells designs with miniaturized elements", in *Proc. IEEE Int. Workshop Antenna Technol. (iWAT)*, Sydney, NSW, Australia, pp. 206-209, Mar. 2019.

[19] L. Zheng *et al*., "Investigating the dual-passbands frequency selective surface with complementary structure", in *Proc. PIERS*, Guangzhou, China, pp. 1494-1496, Aug. 2014.

[20] H. Hassani, J. S. Silva, S. Capdevilla, M. García-Vigueras, J. R. Mosig, "Dual-Band Circularly Polarized Transmitarray Antenna for Satellite Communications at 20/30 GHz", *IEEE Trans. Antennas Propag.*, vol. 67, no, 8, Aug. 2019.

[21] S. A. Matos, J. R. Costa, P. Naseri, E. B. Lima, C. A. Fernandes, N. J. G. Fonseca, "Equivalent Dielectric Description of Transmit-arrays as an efficient and accurate method of analysis", *2020 14th European Conference on Antennas and Propag.*, DOI: 10.23919/EuCAP48036.2020.

[22] C. A. Fernandes, "KH3D_near – User's manual", Version 0.2h, Internal Report Instituto de Telecomunicações, Mar. 2018.

[23] CST Microwave Studio – Computer Simulation Technology: https://www.cst.com, Oct. 2014.

[24] R. F. Harrington, "Time-Harmonic Electromagnetic Fields", Wiley-*IEEE Press*, 2001